Control of an Exoskeleton for Realization of Aquatic Therapy Effects

Kyoungchul Kong, *Member, IEEE*, Hyosang Moon, *Student Member, IEEE*, Doyoung Jeon, *Member, IEEE*, and Masayoshi Tomizuka, *Fellow, IEEE*

***Abstract*—Exoskeletons are attracting great attention as a new means of rehabilitation devices. In such applications, control algorithms of exoskeletons are often inspired by nature for natural and effective assistance for patients. In this paper, a control algorithm inspired by aquatic therapy is introduced. Aquatic therapy provides various beneficial effects for rehabilitation based on useful properties of water, e.g., buoyancy and drag. The proposed controller calculates joint torques equivalent to the buoyant and drag forces. Then, an exoskeleton-type assistive device generates the calculated joint torques to provide the similar effects as aquatic therapy. In this paper, the Sogang University biomedical assist robot is utilized as a testbed. This paper also discusses the mechanical impedance of actuators, which obstructs implementation of controllers in practice. The resistive forces generated by actuators are precisely modeled and compensated to realize the control algorithm inspired by aquatic therapy correctly and effectively.**

***Index Terms*—Aquatic therapy, exoskeleton, healthcare mechatronics, rehabilitation.**

I. Introduction

As MECHATRONIC technologies have merged into applications that improve the quality of lives, researchers have striven to find more effective and practical methods for assisting humans. In recent years, exoskeletons are attracting great attention as a new means of rehabilitation devices for daily use. In such applications, exoskeletons compensate for the lack of muscular forces so that the patients can pursue their daily lives. For examples, Blaya and Herr developed active ankle foot orthosis (AAFO) to assist drop-foot gait by controlling impedance of the device according to gait phases [1], and Nakamura *et al*. introduced wearable walking helper (WWH), which provides supportive joint torques against the gravity [2]. ReWalk (Argo Medical Technologies Ltd., Israel) is a commercialized exoskeleton that assists basic lower limb motions for paraplegic patients [3]. Our research group also introduced exoskeleton for patients and old people by Sogang University (EXPOS) [4], [5] and Sogang University biomedical assist robot (SUBAR) [6], an advanced version of EXPOS.

The design of control algorithms for assisting patients depends on the targeted users of exoskeletons. For patients' rehabilitation, exoskeletons do not necessarily assist the patients' muscular forces; sometimes they resist the human motions to adjust the muscular strength. Since patients can directly feel the control action (i.e., the assistive forces generated by actuators), the control algorithms should generate the control input in an intelligent way such that the patients feel natural assistance without discomfort. In this aspect, control algorithms in human mechatronics are often inspired from nature. For example, the control algorithm in [7] was inspired by a fictitious gain in the human brain. Chugo *et al*. designed a control algorithm inspired by a professional physical therapist for assisting standing and sitting motions [8]. The inspiration from nature makes it easy to design an algorithm that generates natural assistive forces.

In this paper, a control algorithm for rehabilitation is introduced, which is inspired by aquatic therapy. Aquatic therapy is widely accepted as a physical rehabilitative treatment because of the various beneficial properties of water, such as the buoyancy and the drag forces [9]–[11]. Note that the body weight is supported by the buoyancy, which allows patients to practice rehabilitative motions with less stress in the joints. The reduced body weight also implies improved safety, e.g., less impact forces. On the other hand, the drag forces of water introduce resistive forces to the human motion. Since the magnitude of drag forces is related to the velocities of the body, the patients feel as if damping coefficients in their joints are increased. By the passivity theory [12], the increased damping coefficients imply better stability of the human body. Also, the resistive forces help patients to improve the muscular strength. Due to these beneficial effects of water, patients can practice rehabilitative tasks under a safe and stable environment. In this paper, a control algorithm is designed such that the advantages of aquatic therapy can be realized by an exoskeleton system; patients will be able to take advantages of aquatic therapy without being submerged into water in daily lives.

Implementation of control algorithms in exoskeleton systems is challenged by practical problems in hardware, such as mechanical impedance or inherent nonlinearities in actuators [6], [13]. Many researchers have striven to solve such practical problems, for example, Buerger *et al*. introduced a loop shaping method to reduce the actuator impedance [21], and Kong and Tomizuka proposed a robust feedback controller that realizes the ideal force-mode actuation using a rotary series elastic actuator [13]. In this paper, the dynamic characteristics of

Manuscript received June 9, 2009; revised November 19, 2009. First published March 1, 2010; current version published March 31, 2010. Recommended by Guest Editor G. Morel. This paper was presented in part at the 2009 IEEE International Conference on Robotics and Automation, Kobe, Japan.

K. Kong and M. Tomizuka are with the Department of Mechanical Engineering, University of California at Berkeley, Berkeley, CA 94720 USA (e-mail: kckong@me.berkeley.edu; tomizuka@me.berkeley.edu).

H. Moon is with the Department of Mechanical Engineering, Texas A&M University, College Station, TX 77843 USA (e-mail: hsmoon@neo.tamu.edu).

D. Jeon is with the Department of Mechanical Engineering, Sogang University, Seoul 121-742, Korea (e-mail: dyjeon@sogang.ac.kr).

Color versions of one or more of the figures in this paper are available online at http://ieeexplore.ieee.org.

Digital Object Identifier 10.1109/TMECH.2010.2041243

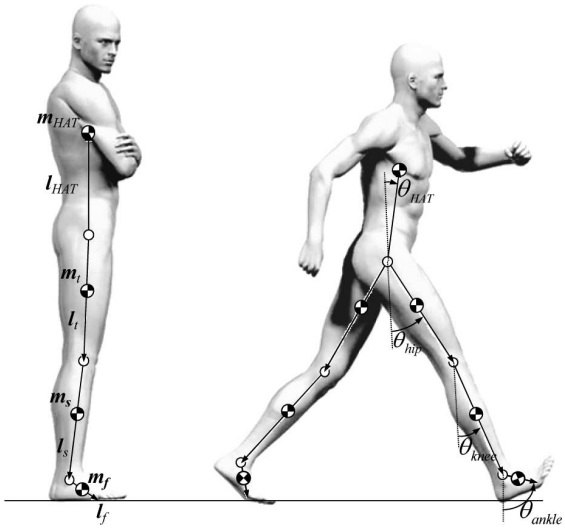

Fig. 1. Biomechanical model of human body.

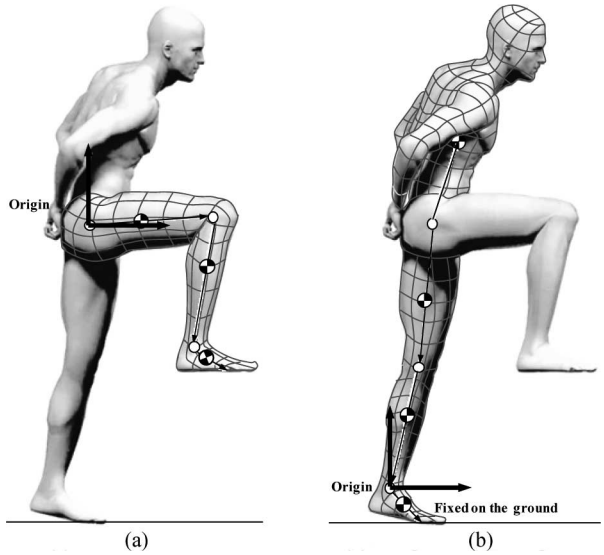

Fig. 2. Two different cases for human joint motions. They consist of (a) a swinging leg (i.e., the three-link pendulum pinned at a hip joint) and (b) HAT with a leg touching the ground (i.e., the four-link inverted pendulum pinned at an ankle joint).

actuators are precisely identified and compensated by a friction compensator.

This paper deals mainly with the following three topics:

1) a control algorithm inspired by aquatic therapy;
2) a human body model and a motion detection algorithm that allows the proposed algorithm to adaptively change parameters according to the human motion phases;
3) implementation of the proposed algorithm; identification of parameters of an actuator used in an exoskeleton system to compensate for undesired actuator dynamics.

The proposed methods are implemented in SUBAR [6] and its effectiveness is verified by experiments.

II. Estimation of Human Joint Torques in Aquatic Therapy Conditions

A. Biomechanical Model of Human Body

In order to estimate assistive joint torques in aquatic therapy, a human body model is utilized in this paper. Many approaches have been studied to model the human body, e.g., a 3-D model based on the Hill muscle model [22] and a human joint model based on anatomy [5]. Since the human body model for the joint torque estimation should be calculated in real time, a simple planar-link model is applied, which consists of seven rigid segments, as shown in Fig. 1. The height and the total body weight of the model are to be determined by the human body parameters. For some human body properties that are difficult to measure accurately, anthropometric rules in [15] can be utilized.

The human body model shown in Fig. 1 is represented in Cartesian coordinates on the sagittal plane. For the sake of simplicity, suppose the following

1) The ground surface is even without inclination.
2) The human body is constituted only by links and masses; any other dynamic characteristics of the human body, such as damping effects, friction in joints, and spring effects of ligaments, are neglected.
3) The head, arms, and trunk (HAT) are treated as one lumped mass.

The leg shows different dynamic characteristics depending on whether or not the foot touches the ground. Even though it is possible to include all seven segments in one model, the human body model is divided into two different models for simplicity (i.e., a stance leg and a swinging leg, as shown in Fig. 2).

In the swinging leg, the hip has the smallest movement among the hip, knee, and ankle. Therefore, the hip joint is set as the reference point [see Fig. 2(a)], and the swinging leg is modeled as a three-link pendulum pivoted at the hip joint.

When the foot is touching the ground (i.e., the stance leg model), either the ankle joint, the heel, or the toe is set as the reference point depending on motion phases. Due to the different reference points, different parameters can be applied to calculate the torques for the same joints. Assuming that the foot is fixed at the ground while touching the ground, the leg is modeled as an inverted pendulum. Since the HAT is supported by the leg touching the ground, the HAT is included in the stance leg model, as shown in Fig. 2(b).

B. Buoyant Forces

Patients feel that their body weight is reduced under water. This is due to the buoyant force. The buoyant force is a very important factor in aquatic therapy, because the body weight is supported by the buoyant forces; patients can move their bodies with less stress in their joints. By Archimedes' principle, the magnitude of buoyant force is equal to the weight of water displaced by the submerged body, while its direction is opposite to the gravity force. Therefore, the volume of each body segment and the density of water are required to estimate the buoyant force. For the sake of simplicity, suppose that the following holds.

1) The mass of the entire body is uniformly distributed (i.e., the mass density is a constant for all body segments).

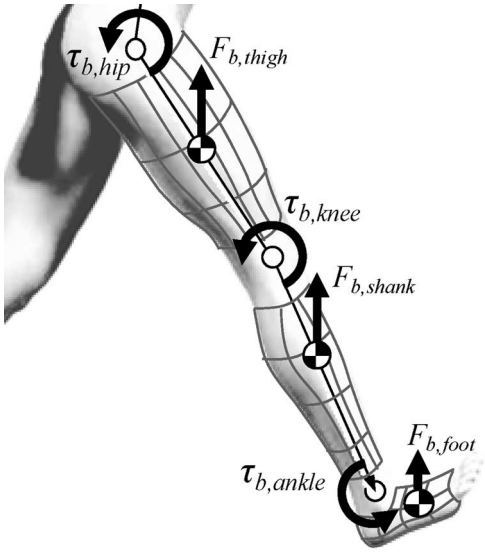

Fig. 3. Schematic plot of buoyant torque on each joint during swinging.

2) The buoyant force is concentrated on the center of mass (COM) of each body segment (see Fig. 3).

With the aforementioned assumptions, the buoyant force exerted on the ith segment, $F_{b,i}$, is obtained as

$$F_{b,i} = \rho_w g V_i \mathbf{e}_{\mathrm{T}} = \frac{\rho_w}{\rho_b} m_i g \mathbf{e}_{\mathrm{T}} \tag{1}$$

where ρ_w is the mass density of water (995.7 kg/m^3 at 30 °C), ρ_b is the mass density of a human body (approximately 1041 kg/m^3 [16]), g and V_i are the gravity acceleration and the volume of the ith segment, respectively, and $\mathbf{e}_{\mathrm{T}}$ is a unit normal vector on the transverse plane. Since ρ_w/ρ_b is constant by the assumption (i.e., $\rho_w/\rho_b \approx 0.956$), the buoyant force $F_{b,i}$ is calculated as the scaled weight of each segment, while its direction is opposite to the gravity force.

To realize the buoyant effects by an exoskeleton system, an assistive joint torque equivalent to the buoyant force in (1) is calculated. Since the human body model is different depending on the ground contact conditions, as shown in Fig. 2, two sets of joint torques are calculated for each leg (i.e., one is by the swinging model [see Fig. 2(a)] and the other one is by the stance model [see Fig. 2(b)]). The interpolation between the two estimates will be discussed in Section III.

Fig. 3 shows the buoyant torques exerted on the knee joint during swinging. In the figure, the two concentrated buoyant forces are exerted on the COM of each segment (i.e., the shank and the foot). In general, the effective joint torques for the swinging leg under water on the sagittal plane are

$$\begin{bmatrix} \tau_{b,\mathrm{ankle}} \\ \tau_{b,\mathrm{knee}} \\ \tau_{b,\mathrm{hip}} \end{bmatrix}_{\mathrm{sw}} = \frac{\beta_b \rho_w g}{\rho_b} \begin{bmatrix} \alpha_f m_f l_f \sin\theta_{\mathrm{ankle}} \\ (\alpha_s m_s + m_f) l_s \sin\theta_{\mathrm{knee}} \\ (\alpha_t m_t + m_s + m_f) l_t \sin\theta_{\mathrm{hip}} \end{bmatrix} + \begin{bmatrix} 0 \\ \tau_{b,\mathrm{ankle}} \\ \tau_{b,\mathrm{knee}} \end{bmatrix}_{\mathrm{sw}} \tag{2}$$

where β_b is an adjustable gain in the range of $0 \le \beta_b \le 1$; the amount of buoyant effect can be adjusted by this gain. The variables g, ρ_w, and ρ_b are same as in (1), and the other variables are as shown in Figs. 1 and 3. Note that the joint torques are calculated in the sequence of the ankle, knee, and hip joints, and are correlated to each other.

Similarly, the effective joint torques for the stance leg are

$$\begin{bmatrix} \tau_{b,\mathrm{hip}} \\ \tau_{b,\mathrm{knee}} \\ \tau_{b,\mathrm{ankle}} \end{bmatrix}_{\mathrm{st}} = \frac{\beta_b \rho_w g}{\rho_b} \begin{bmatrix} \alpha_{\mathrm{HAT}} m_{\mathrm{HAT}} l_{\mathrm{HAT}} \sin\theta_{\mathrm{HAT}} \\ ((1-\alpha_t) m_t + m_{\mathrm{HAT}}) l_t \sin\theta_{\mathrm{hip}} \\ ((1-\alpha_s) m_s + m_t + m_{\mathrm{HAT}}) l_s \sin\theta_{\mathrm{knee}} \end{bmatrix} + \begin{bmatrix} 0 \\ \tau_{b,\mathrm{hip}} \\ \tau_{b,\mathrm{knee}} \end{bmatrix}_{\mathrm{st}}. \tag{3}$$

Note that they are calculated in the reverse way of (2), and different variables are used to calculate the same joint torque [e.g., see $\tau_{b,\mathrm{hip}}$ in (2) and (3)]. Also, it should be noted that (2) and (3) are not functions of time; the assistive joint torques derived by buoyant forces may be effective to compensate for the gravity forces.

For general motions where the swing and stance phases appear alternatively, an appropriate model in either (2) or (3) should be applied according to the ground contact conditions.

C. Drag Forces

Since the drag force of water introduces significant resistive forces, it should be included in the control algorithm inspired by aquatic therapy. The resistive forces under water are mainly due to parasitic drag effects. Major components of the parasitic drag forces include interference drag, form drag, and skin friction [19]. Since the interference drag arises from vortices caused by sharp edges, it is neglected by assuming that the human body has no such sharp edges. Therefore, the drag force is mainly due to the form drag and skin friction, which are induced by the shape, dimension, and surface condition of the human body segment.

Since the drag force is influenced by the flow condition around the body segment, Reynolds' number should be checked prior to the selection of an appropriate drag equation. The Reynolds' number of the ith body segment, Re_i, is

$$\mathrm{Re}_i = \frac{v_i D_i}{\nu_w} \tag{4}$$

where v_i and D_i are the speed and the characteristic dimension of each body segment, respectively, and ν_w refers to dynamic viscosity of water (8.009×10^{-7} m^2/s at 30 °C). For the external flow around the body segment, the critical Reynolds' number that determines transition point between laminar and turbulence is about 100 000 [19]. In the case of normal walking motions, v_i is approximately 1–3 m/s [20], which yields Re_i in the range of 250 000–750 000. Since the flow condition can be considered

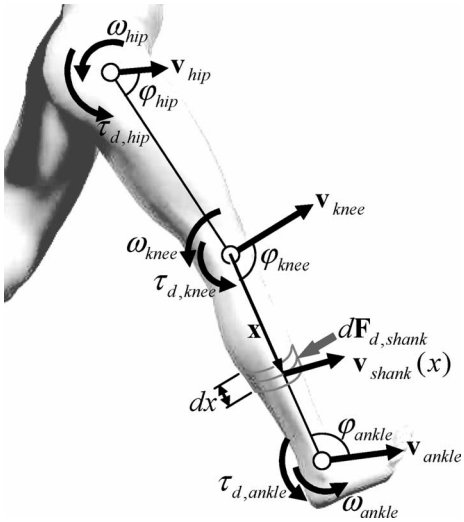

Fig. 4. Schematic plot of drag torque with vector notations. $\mathbf{v}_{\rm hip}$, $\mathbf{v}_{\rm knee}$, and $\mathbf{v}_{\rm ankle}$ are the velocities of hip, knee, and ankle, respectively. $\omega_{\rm hip}$, $\omega_{\rm knee}$, and $\omega_{\rm ankle}$ are the joint angular velocities of hip, knee, and ankle joints, respectively. Also, $\tau_{d,\rm hip}$, $\tau_{d,\rm knee}$, and $\tau_{d,\rm ankle}$ are the effective joint torques induced by the drag effects.

as turbulent, the drag force exerted on a small element of the ith body segment, $d\mathbf{F}_{d,i}$, is estimated by quadratic drag equation, i.e.

$$\begin{aligned} d\mathbf{F}_{d,i} &= -0.5\rho_w C_d \mathbf{v}_i(x)\left|\mathbf{v}_i(x)\right| dA_i \\ &= -\rho_w C_d r_i \mathbf{v}_i(x)\left|\mathbf{v}_i(x)\right| dx_i \end{aligned} \tag{5}$$

where C_d is the drag coefficient of human body (approximately 0.2, the average value of empirical data in [17]), x and r are the position from a joint to the element and the radius of cross section at x, respectively, and A_i is the projected frontal area and is equal to $2r_i x_i$ in (5). Note that the direction of the drag force is opposite to that of the body segment motion, i.e., the drag force resists human motion.

Fig. 4 shows the schematic of drag effects on a knee joint. The velocity of each small element $\mathbf{v}_{\rm shank}(x)$ is calculated based on the velocity of knee joint $\mathbf{v}_{\rm knee}$ and the angular velocity of knee $\boldsymbol{\omega}_{\rm knee}$, i.e.

$$\mathbf{v}_{\rm shank}(x) = \mathbf{v}_{\rm knee} + \boldsymbol{\omega}_{\rm knee} \times \mathbf{x} \tag{6}$$

where $\mathbf{x}$ is the distance from the knee joint to the element (see Fig. 4). Note that (6) is in the vector domain. The magnitude of the effective knee joint torques induced by the drag forces at the small element is

$$\begin{aligned} d\boldsymbol{\tau}_{d,\rm knee} &= \mathbf{x} \times d\mathbf{F}_{d,\rm shank} \\ &= \mathbf{x} \times \left[-\rho_w C_d r_s \mathbf{v}_{\rm shank}(x)\left|\mathbf{v}_{\rm shank}(x)\right|\right] dx. \end{aligned} \tag{7}$$

Substituting (6) into (7),

$$d\boldsymbol{\tau}_{d,\rm knee} = \mathbf{e}_s\left[-\rho_w C_d r_s x(v_{\rm knee}\sin\varphi_{\rm knee} + \omega_{\rm knee} x)^2\right] dx \tag{8}$$

where $\mathbf{e}_s$ is a unit vector on the sagittal plane. The parameters x, $v_{\rm knee}$, and $\omega_{\rm knee}$ are the magnitudes of $\mathbf{x}$, $\mathbf{v}_{\rm knee}$, and $\boldsymbol{\omega}_{\rm knee}$, respectively. $\varphi_{\rm knee}$ is the knee joint angle, as shown in Fig. 4. Integrating (8) over the shank length, the total knee joint torque is

$$\begin{aligned} \tau_{d,\rm knee} &= \int_0^{l_s} d\tau_{d,\rm knee} - \tau_{d,\rm ankle} \\ &= -\rho_w C_d r_s l_s^2 \left[\frac{v_{\rm knee}^2 \sin^2\varphi_{\rm knee}}{2} + \frac{2\omega_{\rm knee} l_s \sin\varphi_{\rm knee}}{3} \right. \\ &\qquad \left. + \frac{\omega_{\rm knee}^2 l_s^2}{4}\right] - \tau_{d,\rm ankle}. \end{aligned} \tag{9}$$

Note that (9) is the effective knee joint torque induced by the drag forces while swinging. Since all of the vectors are on the sagittal plane, the unit vector $\mathbf{e}_s$ was ignored in (9) for simplicity.

In general, the effective joint torques on ankle, knee, and hip joints during swinging are as in (10), shown at the bottom of the page, where $\varphi_{\rm ankle}$, $\varphi_{\rm knee}$, and $\varphi_{\rm hip}$ are as shown in Fig. 4. Note that (10) is calculated from the ankle joint to the hip joint as in (2). Similarly, the effective joint torques in a leg touching the ground are given in (11), shown at the bottom of the page.

$$\begin{bmatrix} \tau_{d,\rm ankle} \\ \tau_{d,\rm knee} \\ \tau_{d,\rm hip} \end{bmatrix}_{\rm sw} = -\rho_w C_d \begin{bmatrix} r_f l_f^2 \left(\frac{v_{\rm ankle}^2 \sin^2\varphi_{\rm ankle}}{2} + \frac{2l_f\omega_{\rm ankle} v_{\rm ankle}\sin\varphi_{\rm ankle}}{3} + \frac{l_f^2\omega_{\rm ankle}^2}{4}\right) \\ r_s l_s^2 \left(\frac{v_{\rm knee}^2 \sin^2\varphi_{\rm knee}}{2} + \frac{2l_s\omega_{\rm knee} v_{\rm knee}\sin\varphi_{\rm knee}}{3} + \frac{l_s^2\omega_{\rm knee}^2}{4}\right) \\ r_t l_t^2 \left(\frac{v_{\rm hip}^2 \sin^2\varphi_{\rm hip}}{2} + \frac{2l_t\omega_{\rm hip} v_{\rm hip}\sin\varphi_{\rm hip}}{3} + \frac{l_t^2\omega_{\rm hip}^2}{4}\right) \end{bmatrix} - \begin{bmatrix} 0 \\ \tau_{d,\rm ankle} \\ \tau_{d,\rm knee} \end{bmatrix}_{\rm sw} \tag{10}$$

$$\begin{bmatrix} \tau_{d,\rm hip} \\ \tau_{d,\rm knee} \\ \tau_{d,\rm ankle} \end{bmatrix}_{\rm st} = -\rho_w C_d \begin{bmatrix} r_{\rm HAT} l_{\rm HAT}^2 \left(\frac{v_{\rm hip}^2 \sin^2\varphi_{\rm hip}}{2} + \frac{2l_{\rm HAT}\omega_{\rm HAT} v_{\rm hip}\sin\varphi_{\rm hip}}{3} + \frac{l_{\rm HAT}^2\omega_{\rm HAT}^2}{4}\right) \\ r_t l_t^2 \left(\frac{v_{\rm knee}^2 \sin^2\varphi_{\rm knee}}{2} + \frac{2l_t\omega_{\rm knee} v_{\rm knee}\sin\varphi_{\rm knee}}{3} + \frac{l_t^2\omega_{\rm knee}^2}{4}\right) \\ r_s l_s^2 \left(\frac{v_{\rm ankle}^2 \sin\varphi_{\rm ankle}}{2} + \frac{2l_s\omega_{\rm ankle} v_{\rm ankle}\sin\varphi_{\rm ankle}}{3} + \frac{l_s^2\omega_{\rm ankle}^2}{4}\right) \end{bmatrix} - \begin{bmatrix} 0 \\ \tau_{d,\rm hip} \\ \tau_{d,\rm knee} \end{bmatrix}_{\rm st} \tag{11}$$

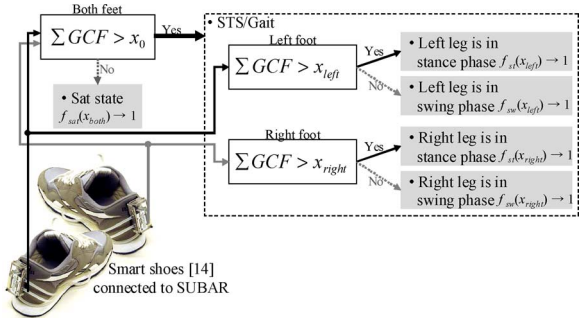

Fig. 5. Structure of motion detection algorithm.

Based on (2), (3), (10), and (11), the desired assistive torques inspired by aquatic therapy are

$$\begin{cases} \mathbf{T}_{\rm sw} = \begin{bmatrix} \tau_{b,\rm hip} \\ \tau_{b,\rm knee} \\ \tau_{b,\rm ankle} \end{bmatrix}_{\rm sw} + \begin{bmatrix} \tau_{d,\rm hip} \\ \tau_{d,\rm knee} \\ \tau_{d,\rm ankle} \end{bmatrix}_{\rm sw} \in \Re^3, \quad \text{for swinging leg} \\ \mathbf{T}_{\rm st} = \begin{bmatrix} \tau_{b,\rm hip} \\ \tau_{b,\rm knee} \\ \tau_{b,\rm ankle} \end{bmatrix}_{\rm st} + \begin{bmatrix} \tau_{d,\rm hip} \\ \tau_{d,\rm knee} \\ \tau_{d,\rm ankle} \end{bmatrix}_{\rm st} \in \Re^3, \quad \text{for stance leg.} \end{cases} \tag{12}$$

Note that the joint torques in (12) are applied to each leg separately. For the left and right legs, the same algorithm is applied to each leg. Moreover, the estimation algorithm requires information on the human motion phases. For this purpose, an algorithm that detects the motion phases is accompanied with the proposed method.

III. Motion Detection Algorithm

As the human feet repeatedly contact the ground, the ground contact conditions change continuously. The smart shoes proposed in [14] are utilized to observe the ground contact conditions. According to the magnitude of the measured ground contract forces (GCFs), the motion phases are detected such that the joint torques in (12) can be calculated for the right motion phase.

Fig. 5 shows the entire motion detection algorithm. Assumed motions include walking, sit-to-stand, and stand-to-sit. Although actual human motions include much more complicated motion phases (e.g., a human gait includes eight motion phases, and six of them exhibit different dynamic responses [7]), increasing the number of motion phases is not practical due to high computation load.

The logic of the motion detection algorithm is as follows.

1) If the sum of all GCFs measured from both feet is less than a threshold (x_0), the current motion is classified as the sat state (i.e., the human is sitting on a chair).
2) While the sum of all GCFs from both feet is larger than the threshold, a leg is in the stance phase (i.e., the foot is touching the ground) if the sum of the GCFs from one foot is larger than a threshold ($x_{\rm left}$ or $x_{\rm right}$).
3) Otherwise, the leg is in the swing phase.

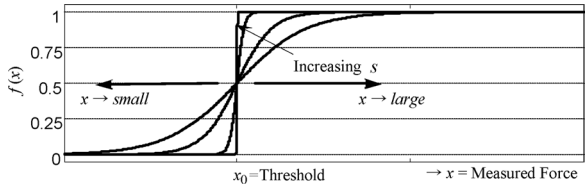

Fig. 6. Fuzzy membership function [14].

Even though a simple threshold method can distinguish the motion phases, a hyperbolic tangent function shown in Fig. 6 is applied in this paper for a smooth and continuous detection of the motion phases. This is reasonable because: 1) human motion phases do not abruptly change and 2) the two different models shown in Fig. 2 should smoothly change in order to avoid sudden jumps in the calculated assistive torques. The likelihood of sitting motion is

$$f_{\rm sat}(x_{\rm both}) = \frac{1}{2}\left[1 - \tanh(s(x_{\rm both} - x_{0,\rm both}))\right] \in [0,1] \tag{13}$$

where $x_{\rm both}$, $x_{0,\rm both}$, and s represent the summation of GCFs measured from the left and right feet, the threshold value, and the sensitivity coefficient, respectively. Note that (13) takes a value close to one if the sum of GCFs is smaller than the threshold. In other words, the human is most likely sitting on a chair if $f_{\rm sat}(x_{\rm both})$ is close to one. Since the function in (13) is symmetric, $f_{\rm STS/Gait}(x_{\rm both})$, the likelihood of the remaining motion phases (i.e., swing and stance phases during walking, sit-to-stand and stand-to-sit motions) is obtained by

$$f_{\rm STS/Gait}(x_{\rm both}) = 1 - f_{\rm sat}(x_{\rm both}) \in [0,1]. \tag{14}$$

Equation (14) returns a value close to one if the sum of GCFs from both feet is greater than the threshold. The shape of likelihood functions in (13) and (14) are shown in Fig. 6. Note that the function returns continuous and smooth values over the entire range, and its slope (i.e., sensitivity) can be easily adjusted by the parameter s without loss of characteristics.

If $f_{\rm sat}(x_{\rm both})$ in (13) is close to zero (i.e., the human is not sitting on a chair), the GCFs from each foot are analyzed to check if each leg is in the swing phase [see Fig. 2(a)] or in the stance phase [see Fig. 2(b)], i.e.

$$f_{\rm st}(x_{\rm each}) = 0.5 f_{\rm STS/Gait}(x_{\rm both})[1 + \tanh(s(x_{\rm each} - x_{0,\rm each}))] \tag{15}$$

$$f_{\rm sw}(x_{\rm each}) = 0.5 f_{\rm STS/Gait}(x_{\rm both})[1 - \tanh(s(x_{\rm each} - x_{0,\rm each}))] \tag{16}$$

where $x_{\rm each}$ and $x_{0,\rm each}$ are the sum of GCFs from each foot and a threshold value, respectively. Since the proposed algorithm in Section II requires only the motion phases of swing and stance during walking, the summation of all GCFs in each foot is used for the motion detection. Note that $f_{\rm STS/Gait}(x_{\rm both})$ is multiplied in (15) and (16), because these likelihoods are meaningful only when the human is walking, standing up, or sitting down. If the human is sitting, $f_{\rm STS/Gait}(x_{\rm both})$ is close to zero, and thus, $f_{\rm st}$ $(x_{\rm each})$ and $f_{\rm sw}$ $(x_{\rm each})$ are close to zero.

Notice that the sum of the likelihoods of the three motion phases is one, i.e., $f_{\mathrm{STS/Gait}}(x_{\mathrm{both}}) + f_{\mathrm{st}}(x_{\mathrm{each}}) + f_{\mathrm{sw}}(x_{\mathrm{each}}) = 1$ for each leg.

To obtain the desired assistive torque from the two different models in (12), the likelihoods of motion phases are utilized as weighting factors. A weighting vector $\mathbf{F}$, which consists of the likelihoods of motions, is defined as

$$\mathbf{F}_{\mathrm{left}} = [\, f_{\mathrm{st}}(x_{\mathrm{left}}) \quad f_{\mathrm{sw}}(x_{\mathrm{left}}) \quad f_{\mathrm{sat}}(x_{\mathrm{both}}) \,]^{\mathrm{T}} \in \Re^3 \tag{17}$$

$$\mathbf{F}_{\mathrm{right}} = [\, f_{\mathrm{st}}(x_{\mathrm{right}}) \quad f_{\mathrm{sw}}(x_{\mathrm{right}}) \quad f_{\mathrm{sat}}(x_{\mathrm{both}}) \,]^{\mathrm{T}} \in \Re^3. \tag{18}$$

Note that the components in $\mathbf{F}$'s change smoothly and continuously according to the ground contact conditions. Consider a joint torque matrix, $\mathbf{J}$, i.e.

$$\mathbf{J}_{\mathrm{left}} = [\, \mathbf{T}_{\mathrm{st,left}} \quad \mathbf{T}_{\mathrm{sw,left}} \quad \mathbf{T}_{\mathrm{sat}} \,] \in \Re^{3\times 3} \tag{19}$$

$$\mathbf{J}_{\mathrm{right}} = [\, \mathbf{T}_{\mathrm{st,right}} \quad \mathbf{T}_{\mathrm{sw,right}} \quad \mathbf{T}_{\mathrm{sat}} \,] \in \Re^{3\times 3} \tag{20}$$

where each column vector $\mathbf{T}$ represents the desired assistive torques and is as defined in (12). Assuming that the human is fully relaxed in the sat state, $\mathbf{T}_{\mathrm{sat}}$ is set to be zero vector, i.e., $\mathbf{T}_{\mathrm{sat}} = [0\ 0\ 0]^{\mathrm{T}}$. $\mathbf{T}_{\mathrm{st,left}}$ is the desired assistive torques of left leg in the stance phase and $\mathbf{T}_{\mathrm{sw,left}}$ is those of left leg during swinging. A joint torque matrix for the right leg $\mathbf{J}_{\mathrm{right}}$ is also defined similarly.

Finally, the desired assistive torques for each leg are obtained by multiplying (19) by (17), or (20) by (18), i.e.,

$$\mathbf{T}_{a,\mathrm{left}} = \mathbf{J}_{\mathrm{left}}\mathbf{F}_{\mathrm{left}} \in \Re^3 \tag{21}$$

$$\mathbf{T}_{a,\mathrm{right}} = \mathbf{J}_{\mathrm{right}}\mathbf{F}_{\mathrm{right}} \in \Re^3. \tag{22}$$

Note that $\mathbf{T}_{\mathrm{sw}}$ and $\mathbf{T}_{\mathrm{st}}$ in each $\mathbf{J}$ are continuously calculated in real time regardless of the human motion phases. Then, an appropriate assistive joint torque set is obtained by interpolating the calculated values according to the human motion phases. Since the components in $\mathbf{F}$ change smoothly and continuously, the resultant assistive torques calculated by (21) and (22) are smooth and continuous.

IV. Implementation in SUBAR System

A. SUBAR System

The proposed algorithm is implemented in SUBAR [6]. The SUBAR system consists of two major parts: an orthosis worn by a patient and a caster walker (see Fig. 7). The caster walker plays the role of a robotic physical therapist; it guides proper motions while providing assistive forces to the patient. SUBAR provides a user with assistive joint torques by electric motors in the robot arms. A Pentium 4-level PC is embedded in SUBAR and the main control algorithm is run at the sampling rate of 1 kHz. The controller structure is flexible such that the desired assistive joint torques can be determined either by a trajectory or by a real-time feedback control algorithm. For more information on the mechanical design of SUBAR, see [6].

B. Actuator Dynamics Compensation

The desired assistive torque calculated by the proposed algorithms in Sections II and III is generated by actuators for physically assisting humans. However, the generation of a precise torque is challenged by practical problems in actuators, such as mechanical impedances or inherent nonlinearities.

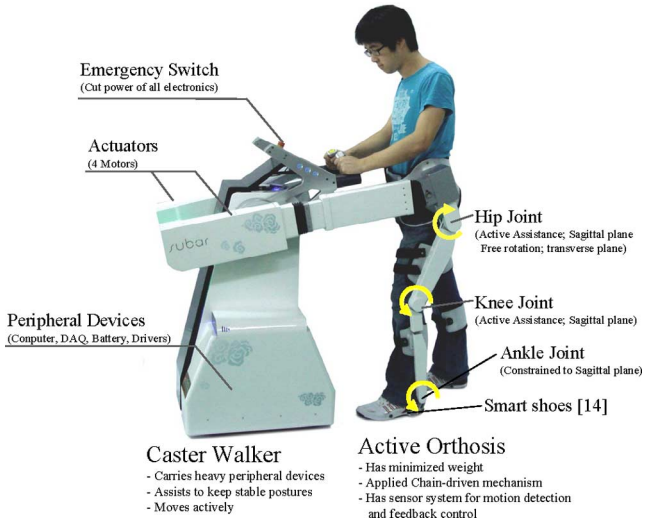

Fig. 7. SUBAR [6].

Suppose that the torque generated by an electric motor τ_{out} is a function of the control input u, the angular velocity of the rotor ω, and the angular acceleration of the rotor α, i.e.

$$\begin{aligned}\tau_{\mathrm{out}} &= f(u, \omega, \alpha) \\ &= au + b\,\mathrm{sgn}(\omega) + c\omega + I\alpha\end{aligned} \tag{23}$$

where a, b, and c are the torque constant of the motor, the magnitude of the Coulomb friction, and the damping coefficient, respectively, and I is the rotor inertia. Notice that $b = 0$, $c = 0$, and $I = 0$ in case of an ideal actuator.

Based on (23), the desired assistive torques are modified to compensate for the actuator dynamics. Since it is desirable that τ_{out} is the same as the desired torques determined by (21) or (22), the control input $\mathbf{U}$ for each leg is determined by

$$\mathbf{U} = \mathbf{A}^{-1}[\mathbf{T} - \mathbf{B}\,\mathrm{sgn}(\Omega) - \mathbf{C}\Omega - \mathbf{I}\dot{\Omega}] \in \Re^3 \tag{24}$$

where $\mathbf{U}$ is the control input vector for three actuators for the hip, knee, and ankle, $\mathbf{A} = \mathrm{diag}[a, a, a]$, $\mathbf{T}$ is the desired assistive torques, $\mathbf{C} = \mathrm{diag}[c, c, c]$, $\mathbf{I} = \mathrm{diag}[I, I, I]$, and $\Omega = [\omega_{\mathrm{hip}}, \omega_{\mathrm{knee}}, \omega_{\mathrm{hip}}]^{\mathrm{T}}$. The parameters a, b, c, and I are as defined in (23). It is assumed that three identical actuators are used to assist the hip, knee, and ankle joints. Since Ω is obtained from encoder measurements in real time, (24) takes the form of a feedback compensation method.

C. Overall Control Structure

The overall control scheme including the assistive torque generator (see Section II), the motion detection algorithm (see Section III), and the friction compensator (see Section IV-B) is as follows:

1) First, the joint angles and the angular velocities are measured by sensors in the exoskeleton. Also, the GCFs are measured by the smart shoes.

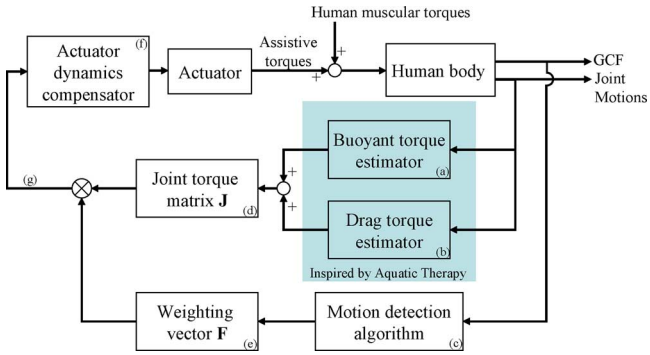

Fig. 8. Block diagram of overall control structure. (a) See (2) and (3). (b) See (10) and (11). (c) Discussed in Section III. (d) See (19) and (20). (e) See (17) and (18). (f) See Section IV-B.

2) Second, the desired assistive torques are calculated by algorithms in (2), (3), (10), and (11) [see Fig. 8(a) and (b)], regardless of the motion phases. In the joint torque matrices $\mathbf{J}_{\mathrm{left}}$ and $\mathbf{J}_{\mathrm{right}}$ all possible joint torques calculated by all human model sets are included.
3) The GCFs are processed by a motion detection algorithm [see Fig. 8(c)] such that the likelihood of each motion phase is estimated.
4) Utilizing the estimated likelihoods as weighting factors, the calculated joint torques in $\mathbf{J}_{\mathrm{left}}$ and $\mathbf{J}_{\mathrm{right}}$ are interpolated, and the desired assistive torques are determined [see Fig. 8(g)].
5) The desired assistive torques are modified by a friction compensator in (24) [see Fig. 8(f)].
6) Finally, the assistive torques are generated by actuators.

V. Controller Verification

A. Assistive Torque Generation Without Actuation Force

Prior to applying the assistive forces to a human subject, the control algorithm was implemented without actuators to check stability and performance.

The orthosis of SUBAR can be freely moved without large resistance when the power transmission mechanism is disconnected. To verify the proposed algorithms, a healthy male subject wore SUBAR, and performed sitting and standing motions, as well as walking motions. In experiments, the relative joint angles were acquired from rotary position sensors installed at the hip, knee, and ankle joints. Also, the GCF signals were measured from the heel and the metatarsal head of both feet using the smart shoes. The proposed algorithms were computed in real time.

Comparing assistive torques generated by the proposed method with experimental data measured during actual aquatic therapy may be a good way to validate the effectiveness of the proposed method. However, it should be noted that there is no direct method to measure the human joint torques, in particular, under water. Although alternative methods, such as vision-based motion capture systems and electromyography, provide estimates of joint torques, they are based on inverse dynamics methods or unreliable biomedical signals in limited conditions. Miyoshi *et al.* suggested a method to quantify the joint torques during walking in water [23], [24], but they also utilized the inverse dynamics method based on the ground contact forces and kinematic data measured from a motion analysis system on the ground. Therefore, utilizing the inverse dynamics of a simplified body model used in this paper is a common way to estimate the joint torques in human motions.

In Fig. 9, the experimental results for one cycle of sitting and standing motions are shown. In the computation of the buoyant torque, the adjustable gain β_b was set to 0.5. The motions of the subject are depicted in Fig. 9(a). The encoders installed at each joint of SUBAR measure the relative angles between body segments, and the relative angles of the hip, knee, and ankle joints are presented in Fig. 9(b). Note that the subject was sitting on a chair from 0 to 0.8 s and from 5 to 6 s. The likelihoods of each motion phase detected based on the GCF signals are shown in Fig. 9(c). As expected, the likelihood of the sat state $f_{\mathrm{sat}}(x)$ was close to one when the subject was sitting on a chair. The buoyant torque, the drag torque, and their summation are shown in Fig. 9(d)–(f). Notice that the calculated knee joint torques are negative, which implies that the assistive torques were generated to support the body weight against the gravity.

When the subject was sitting down (i.e., the seat loading phase of stand-to-sit motion) or standing up (i.e., the seat unloading phase of sit-to-stand motion), the magnitude of the assistive torques abruptly changed, as shown in Fig. 9(d)–(f) (see 0.5–1.5 and 4.5–5.5 s in the figure]. Note that the generated assistive torques were still smooth and continuous even in the transient points due to the smooth and continuous detection of the motion phases.

The standing and sitting motions require large joint torques to lift or lower the body weight against the gravity. As shown in Fig. 9(d)–(f), the buoyant torques play an important role to support the body weight. The drag torques were small, because the speeds of the sitting and standing motions were slow. The amount of the buoyant torques could be adjusted by changing the gain β_b according to each subject's physical conditions. This enables each patient to be assisted such that their muscular strength can be recovered effectively, which is impossible in real aquatic therapy.

B. Human Subject Experiment

Since performance of the proposed method was verified in the previous section, actuators are activated and assistive forces are applied to a healthy human subject in this section. The adjustable gain for buoyancy effect β_b was set to 0.3, i.e., 30% of buoyant effect is to be realized.

Fig. 10 shows the experimental results for one cycle of sitting and standing motions. In Fig. 10(a), the subject was standing up and sitting down. The GCF measurements are shown in Fig. 10(b). Note that the sum of all GCFs significantly decreased when the subject was sitting [e.g., see periods 0–2 and 10–12 s in the figure]. Fig. 10(c) shows the likelihoods detected by the motion detection algorithm. As expected, the likelihood of the sat state was close to one when the sum of all GCFs was small. The assistive torques calculated by the buoyant and

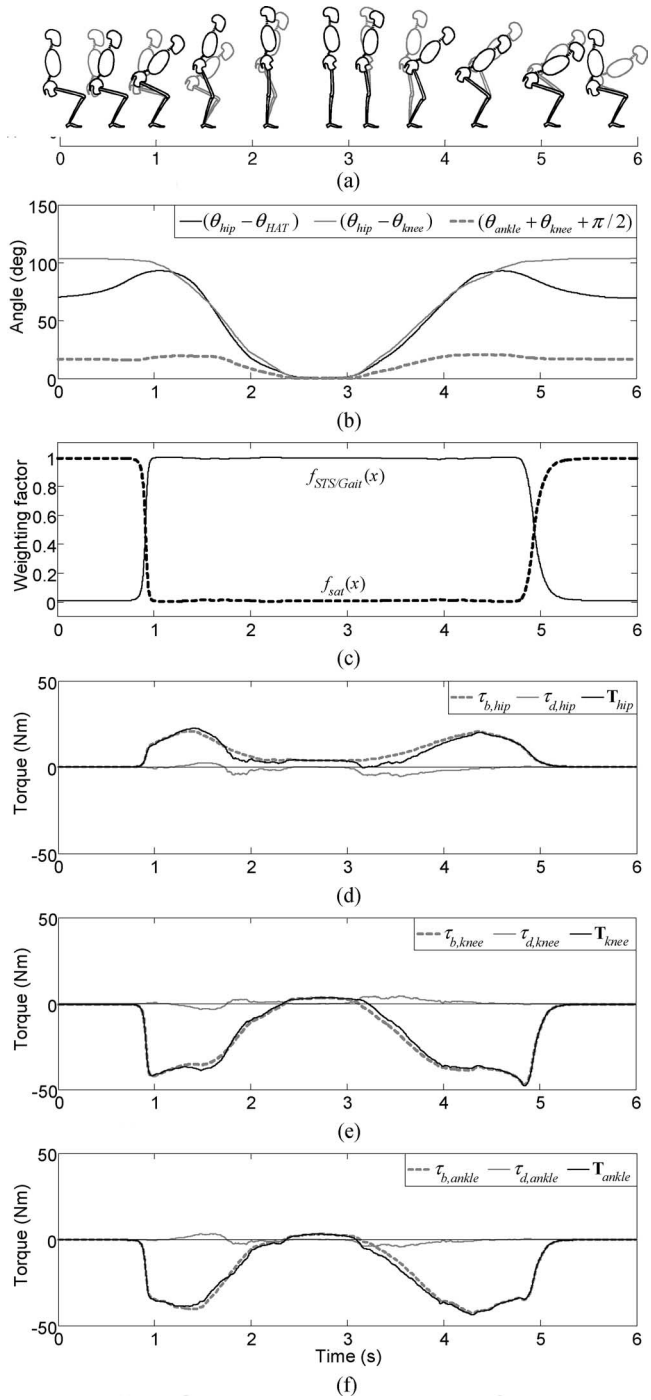

Fig. 9. Assistive torque generation for one cycle of sit-to-stand and stand-to-sit motions. The figures share the same x-axis, i.e., time (in seconds). (a) Sit-to-stand and stand-to-sit motions. (b) Hip, knee, and ankle joint angles. (c) Detection of likelihoods of the STS and sat states. (d) Computed assistive torques for the hip joint. (e) Computed assistive torques for the knee joint. (f) Computed assistive torques for the ankle joint.

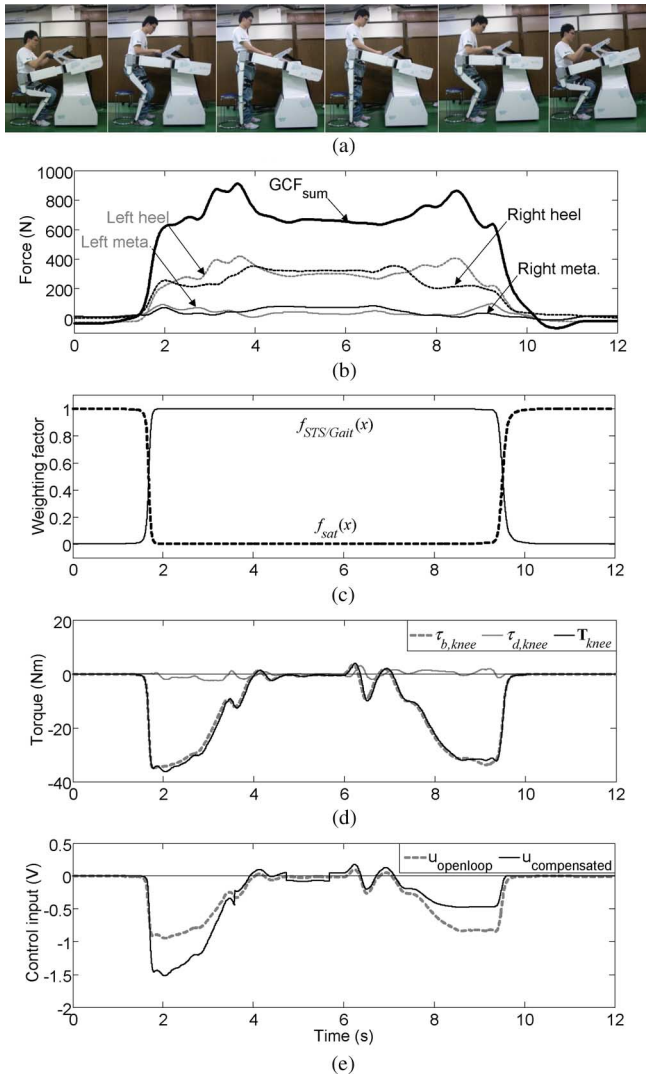

Fig. 10. Experimental results for one cycle of STS motion. All graphs share the same x-axis. (a) Sit-to-stand and stand-to-sit motion. (b) GCFs from each foot ($\mathrm{GCF_{sum}}$ is a sum of all GCFs from both feet). (c) Detection of STS/gait and sat state. (d) Computed assistive torques on a knee joint. (e) Control input on a knee joint.

the drag force models in Section II are shown in Fig. 10(d). It should be noted that the generated torques were smooth and continuous even in phase transition periods [see 1.5–2 and 9–10 s in Fig. 10(d)], which implies that the discomfort, which would be caused by abrupt changes in applied torques, was minimal. Note that the generated assistive torques take the same pattern as in Fig. 9. Fig. 10(e) shows the modified assistive torque signals considering the actuator dynamics as in (25). Note that the magnitude of the modified control input was smaller than the original signal when the subject was sitting down [see between 6 and 10 s in Fig. 10(e)], because both assistive torques and resistive torques by actuator impedance were in the same direction.

The experimental results for walking motions are presented in Fig. 11. The likelihoods of stance and swing phases were detected smoothly and continuously in real time, as shown in Fig. 11(c). As discussed in the previous section, the magnitude of the buoyant torque in the stance phase was larger than in the swing phase [see between 3.5 and 5 s in Fig. 11(d)]. This helps the knee joint to support the whole body weight during the stance phase; note that the knee joint torque was generated in the extension direction during the stance phase.

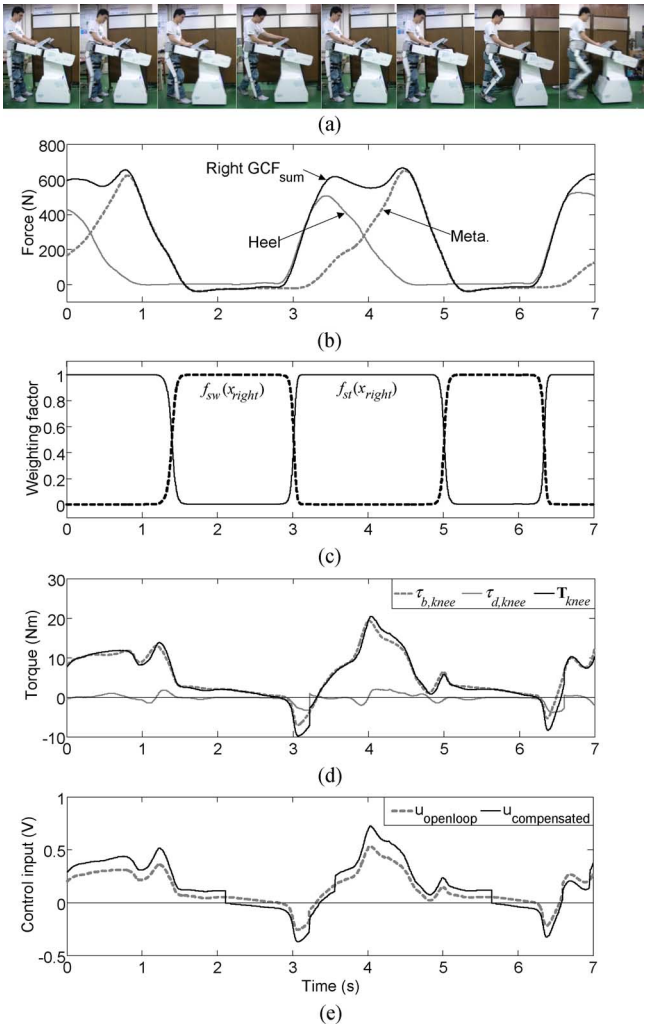

Fig. 11. Experimental results for gait motions. All graphs share the same x-axis. (a) Gait motion. (b) GCFs from the right foot and their summation. (c) Detection of likelihoods of the stance and swing phases. (d) Computed assistive torques for the knee joint. (e) Control input for the knee joint.

Drag torques resisted the subject's motion. Since the magnitude of the drag torque is proportional to the velocity of body segments, high speed motions resulted in large resistive forces. Therefore, the subject could not move fast due to the resistive forces. Such effects were effective to increase the stability of motion and improve the muscular strength.

VI. Summary and Future Work

In order to generate natural assistive forces for rehabilitation, a control algorithm inspired by aquatic therapy was introduced. For the realization of aquatic therapy effects, the buoyant and the drag forces were estimated by two human body models. To switch the body models according to the motion phases, the ground contact forces were measured by the smart shoes and analyzed by a motion detection algorithm. The detection algorithm estimated the likelihoods of each motion phase smoothly and continuously, which enable a smooth and continuous transition of the human body model. The proposed methods were verified by experiments.

In the proposed method, only a few motion phases of the lower extremity were considered: swing and stance phases during walking, and sit-to-stand and stand-to-sit phases during sitting. Although the assumed motion phases may cover most of the normal motion patterns, the limited number of assumed motion phases certainly creates challenges in emulation of natural aquatic therapy effects. In the future work, more motion phases will be considered for more natural assistance and rehabilitation.

Currently, the SUBAR system provides assistive joint torques only. However, the effects of aquatic therapy cannot be fully realized with only the joint torques. For example, when a patient is standing up, the weight of the trunk should be supported to reduce the stresses in joints. Therefore, the mechanical design of SUBAR is being improved such that the robot arms can support the human body weight.

The proposed method is now in preparation for the clinical verification to verify the following objectives: 1) to provide patients with a comfortable and safe assistance using an exoskeleton robot and 2) to help patients to take advantage of aquatic therapy conveniently in daily lives.

References

[1] J. Blaya and H. Herr, "Adaptive control of a variable-impedance ankle-foot orthosis to assist drop-foot gait," *IEEE Trans. Neural Syst. Rehabil. Eng.*, vol. 12, no. 1, pp. 24–31, Mar. 2004.

[2] T. Nakamura, K. Saito, Z. Wang, K. Kosuge, and M. Tajika, "Human cooperative motion adapted wearable anti-gravity muscle support system," in *Proc. IEEE/RSJ Int. Conf. Intell. Robots Syst. (IROS 2006)*, pp. 1843–1848.

[3] Argo Medical Technologies Ltd., Haifa, Israel. (2009). [Online]. Available: http://www.argomedtec.com

[4] K. Kong and D. Jeon, "Design and control of an exoskeleton for the elderly and patients," *IEEE/ASME Trans. Mechatronics*, vol. 11, no. 4, pp. 428–432, Aug. 2006.

[5] A. Maciel, L. P. Nedel, and C. M. D. S. Freitas, "Anatomy-based joint models for virtual human skeletons," in *Proc. IEEE Int. Conf. Comput. Animat. (CA 2002)*, pp. 220–224.

[6] K. Kong, H. Moon, B. Hwang, D. Jeon, and M. Tomizuka, "Impedance compensation of SUBAR for back-drivable force mode actuation," *IEEE Trans. Robot.*, vol. 25, no. 3, pp. 512–521, Jun. 2009.

[7] K. Kong and M. Tomizuka, "Control of exoskeletons inspired by fictitious gain in human model," *IEEE/ASME Trans. Mechatronics*, vol. 14, no. 6, pp. 689–698, 2009.

[8] D. Chugo, W. Matsuoka, S. Jia, and K. Takase, "Rehabilitation walker system with standing assistance device," in *Proc. IEEE Int. Conf. Mech. Autom. (ICMA 2007)*, pp. 2177–2182.

[9] W. E. Prentice and M. L. Voight, *Techniques in Musculoskeletal Rehabilitation*. New York: McGraw-Hill, 2001.

[10] R. S. Hinman, S. E. Heywood, and A. R. Day, "Aquatic physical therapy for hip and knee osteoarthritis: Results of a single-blind randomized controlled trial," *Phys. Ther.*, vol. 87, no. 1, pp. 32–43, 2007.

[11] N. Kesiktas, N. Paker, N. Erdogan, G. Gülsen, D. Biçki, and H. Yilmaz, "The use of hydrotherapy for the management of spasticity," *Neurorehabil. Neural Repair*, vol. 18, no. 4, pp. 268–273, 2004.

[12] J. Ryu, D. Kwon, and B. Hannaford, "Stability guaranteed control: Time domain passivity approach," *IEEE Trans. Control Syst. Technol.*, vol. 12, no. 6, pp. 860–868, Nov. 2004.

[13] K. Kong, J. Bae, and M. Tomizuka, "Control of rotary series elastic actuator for ideal force mode actuation in human–robot interaction applications," *IEEE/ASME Trans. Mechatronics*, vol. 14, no. 1, pp. 105–118, Feb. 2009.

[14] K. Kong and M. Tomizuka, "A gait monitoring system based on air pressure sensors embedded in a shoe," *IEEE/ASME Trans. Mechatronics*, vol. 14, no. 3, pp. 358–370, Jun. 2009.

[15] D. Winter, *Biomechanics and Motor Control of Human Movement*. Malden, MA: Wiley–Interscience, 1990.

[16] J. H. Wilmore and A. R. Behnke, "An anthropometric estimation of body density and lean body weight in young women," *Amer. J. Clin. Nutr.*, vol. 23, no. 3, pp. 267–274, 1970.
[17] T. Pöyhönen, K. L. Keskinen, A. Hautala, and E. Mälkiä, "Determination of hydrodynamic drag forces and drag coefficients on human leg/foot model during knee exercise," *Clin. Biomech.*, vol. 15, no. 4, pp. 256–260, 2000.
[18] M. Kothari, J. G. Webster, W. J. Tompkins, J. J. Wertsch, and P. Bachy-Rita, "Capacitive sensors for measuring the pressure between the foot and shoe," in *Proc. IEEE Int. Conf. Eng. Med. Biol. Soc. (EMBS)*, 1988, pp. 805–806.
[19] A. J. Smits, *A Physical Introduction to Fluid Mechanics*. New York: Wiley, 2000.
[20] A. E. Minetti and F. Saibene, "Mechanical work rate minimization and freely chosen stride frequency of human walking: A mathematical model," *J. Exp. Biol.*, vol. 170, pp. 19–34, 1992.
[21] S. P. Buerger and N. Hogan, "Complementary stability and loop shaping for improved human–robot interaction," *IEEE Trans. Robot.*, vol. 23, no. 2, pp. 232–244, Apr. 2007.
[22] T. Komura, Y. Shinagawa, and T. L. Kunii, "Calculation and visualization of the dynamic ability of the human body," *J. Vis. Comput. Animat.*, vol. 10, pp. 57–78, 1999.
[23] T. Miyoshi, T. Shirota, S. Yamamoto, K. Nakazawa, and M. Akai, "Lower limb joint moment during walking in water," *Disabil. Rehabil.*, vol. 25, no. 21, pp. 1219–1223, 2003.
[24] T. Miyoshi, T. Shirota, S. Yamamoto, K. Nakazawa, and M. Akai, "Functional roles of lower-limb joint moments while walking in water," *Clin. Biomech.*, vol. 20, no. 2, pp. 194–201, 2005.
[25] K. Kong, H. Moon, B. Hwang, D. Jeon, and M. Tomizuka, "Robotic rehabilitation treatments: Realization of aquatic therapy effects in exoskeleton systems," in *Proc. IEEE Int. Conf. Robot. Autom. (ICRA)*, 2009, pp. 1923–1928.

Kyoungchul Kong (S'04–M'09) received the B.Eng. degree in mechanical engineering (*summa cum laude*) and the B.S. degree in physics, both in 2004, and the M.S. degree in mechanical engineering in 2006 from Sogang University, Seoul, Korea, and the Ph.D. degree in mechanical engineering from the University of California, Berkeley, in 2009.

He is currently a Postdoctoral Researcher at the University of California, Berkeley. He has authored or coauthored more than 40 technical articles in journals and conference proceedings in the area of mechatronics including human–robot interaction and assistive systems. His current research interests include design, modeling and control of mechatronic systems with emphasis on betterment of quality of human life.

Dr. Kong was the recipient of the Best Student Paper Award at the IEEE Conference on Advanced Intelligent Mechatronics (AIM) in 2008, the Best Paper Award in the Division of Dynamic Systems and Control at the KSME Annual Conference in 2005, and the Best Poster Award at the 3rd Center of Intelligent Robot Workshop in 2005.

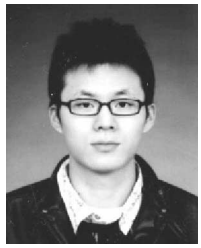

Hyosang Moon (S'08) received the B.Eng. degree in mechanical engineering in 2007 from Sogang University, Seoul, Korea, where he is currently working toward the M.S. degree in mechanical engineering.

His current research interests include design and control of human-interactive robotics such as rehabilitation robots and exoskeleton systems.

Doyoung Jeon (S'86–M'92) received the B.S. degree from Seoul National University, Seoul, Korea, in 1984, and the M.S. and Ph.D. degrees from the University of California, Berkeley, in 1986 and 1991, respectively, all in mechanical engineering.

In 1994, he joined the Department of Mechanical Engineering, Sogang University, Seoul, Korea. His current research interests include the general areas of control systems, such as exoskeletal robots, rehabilitation robots, capsule endoscopes, and servo control of advanced manufacturing machines.

Prof. Jeon was the Dean of Research at Sogang University from 2004 to 2005 and served as a Committee Member of the Korean Presidential Advisory Council on Science and Technology from 2005 to 2006, and the Korean Presidential Commission on Policy Planning from 2002 to 2008.

Masayoshi Tomizuka (M'86–SM'95–F'97) received the B.S. and M.S. degrees from Keio University, Tokyo, Japan, in 1968 and 1970, respectively, and the Ph.D. degree from Massachusetts Institute of Technology, Cambridge, all in mechanical engineering.

In 1974, he joined the Department of Mechanical Engineering, University of California, Berkeley, where he is currently the Cheryl and John Neerhout Jr. Distinguished Professor Chair. His current research interests include optimal and adaptive control, digital control, signal processing, motion control, and control problems related to robotics, machining, manufacturing, and information storage devices and vehicles.

Prof. Tomizuka was the Editor-in-Chief of the IEEE/ASME TRANSACTIONS ON MECHATRONICS from 1997 to 1999. He is a Fellow of the ASME and the SME. He was the recipient of the Charles Russ Richards Memorial Award (ASME, 1997), the Rufus Oldenburger Medal (ASME, 2002), and the John R. Ragazzini Award (2006).